

hep-ph/0204093
ANL-HEP-PR-02-027
FERMILAB-Pub-02/062-T
ILL-(TH)-02-3

October 22, 2018

Higgs-Boson Production in Association with a Single Bottom Quark

J. Campbell¹, R. K. Ellis², F. Maltoni³, and S. Willenbrock³

¹High Energy Physics Division, Argonne National Laboratory
Argonne, IL 60439

²Theoretical Physics Department, Fermi National Accelerator Laboratory
P. O. Box 500, Batavia, IL 60510

³Department of Physics, University of Illinois at Urbana-Champaign
1110 West Green Street, Urbana, IL 61801

Abstract

Higgs bosons from an extended Higgs sector, such as a two-Higgs-doublet model, can have greatly enhanced coupling to the bottom quark. Producing such a Higgs boson in association with a single high- p_T bottom quark via $gb \rightarrow hb$ allows for the suppression of backgrounds. Previous studies have instead used $gg, q\bar{q} \rightarrow b\bar{b}h$ as the production mechanism, which is valid only if both b quarks are at high p_T . We calculate $gb \rightarrow hb$ at next-to-leading order in QCD, and find that it is an order of magnitude larger than $gg, q\bar{q} \rightarrow b\bar{b}h$ at the Fermilab Tevatron and the CERN Large Hadron Collider. This production mechanism improves the prospects for the discovery of a Higgs boson with enhanced coupling to the b quark.

1 Introduction

The Higgs boson couples to fermions with strength m_f/v , where $v = (\sqrt{2}G_F)^{-1/2} \approx 246$ GeV is the vacuum expectation value of the Higgs field. Its Yukawa coupling to bottom quarks ($m_b \approx 5$ GeV) is thus very weak, leading to very small cross sections for associated production of the Higgs boson and bottom quarks at the Fermilab Tevatron [1] and the CERN Large Hadron Collider (LHC) [2]. However, this Yukawa coupling could be considerably enhanced in extensions of the standard model with more than one Higgs doublet, thereby increasing this production cross section [2]. For example, in a two-Higgs-doublet model, the Yukawa coupling of some or all of the Higgs bosons (h^0, H^0, A^0, H^\pm) to the bottom quark could be enhanced for large values of $\tan\beta = v_2/v_1$, where v_1 is the vacuum expectation value of the Higgs doublet that couples to the bottom quark.

The dominant subprocess for the production of a Higgs boson via its coupling to bottom quarks is $b\bar{b} \rightarrow h$ (Fig. 1),¹ where the b quarks reside in the proton sea [2, 3]. The b -quark sea is generated from gluons splitting into nearly collinear $b\bar{b}$ pairs. When one member of the pair initiates a hard-scattering subprocess, its partner tends to remain at low p_T and to become part of the beam remnant. Hence the final state typically has no high- p_T bottom quarks. This subprocess may be useful to discover a Higgs boson for large $\tan\beta$ in the decay mode $h \rightarrow \tau^+\tau^-$ at the Tevatron and the LHC [4, 5], and $h \rightarrow \mu^+\mu^-$ at the LHC [5, 6, 7]. The decay mode $h \rightarrow b\bar{b}$ is not distinguishable from the overwhelming background $gg, q\bar{q} \rightarrow b\bar{b}$.

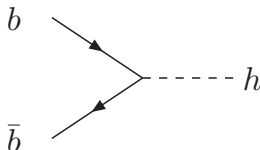


Figure 1: Production of the Higgs boson via $b\bar{b} \rightarrow h$. There are typically no high- p_T bottom quarks in the final state.

If one instead demands that at least one b quark be observed at high p_T , then the leading-order subprocess for associated production of the Higgs boson and bottom quarks is $gb \rightarrow hb$ (Fig. 2) [8, 9].² The presence of a high- p_T bottom quark in the final state has distinct phenomenological advantages since it can be tagged with reasonably high efficiency. In the case of $h \rightarrow \tau^+\tau^-$, $\mu^+\mu^-$ the b quark can be used to reduce backgrounds and to identify the Higgs-boson production mechanism [5, 10, 11]. The trade-off is that the cross section for $gb \rightarrow hb$, with the b quark at high p_T , is less than that of $b\bar{b} \rightarrow h$.

If the Higgs boson decays via $h \rightarrow b\bar{b}$, the presence of an additional high- p_T bottom quark in the final state is essential in order to separate the signal from backgrounds [12, 13]. Recent analyses are based on the subprocess $gg, q\bar{q} \rightarrow b\bar{b}h$ (Fig. 3), and demand a final state with four jets, with either at least three b tags, or with four b tags [5, 11, 14, 15, 16, 17].

¹We use h to denote a generic Higgs boson. In a two-Higgs-doublet model, h may denote any of the neutral Higgs bosons (h^0, H^0, A^0).

²This includes the charge-conjugate subprocess $g\bar{b} \rightarrow h\bar{b}$. All charge-conjugate subprocesses are understood throughout this paper.

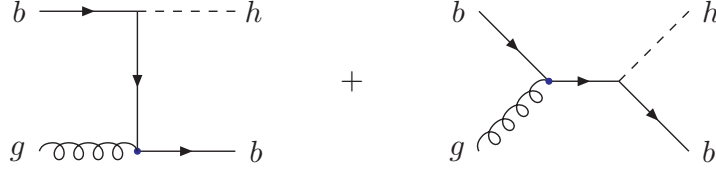


Figure 2: Associated production of the Higgs boson and a single high- p_T bottom quark.

However, the cross section for this subprocess is less than that of $gb \rightarrow hb$. We therefore suggest that it may be advantageous to search for $h \rightarrow b\bar{b}$ by demanding just three jets in the final state, all of which are b tagged [12, 13]. The three-jet final state will have bigger backgrounds than the four-jet final state, but the significance of the signal (S/\sqrt{B}) is likely to increase.

It is only valid to use $gg, q\bar{q} \rightarrow b\bar{b}h$ as the production subprocess when both b quarks are at high p_T . If only one of the b quarks is at high p_T [5, 12, 13], the integration over the momentum of the other b quark yields a factor $\ln(m_h/m_b)$ which invalidates perturbation theory. Our calculation of $gb \rightarrow hb$ sums these logarithms to all orders, and results in a well-behaved perturbation series.

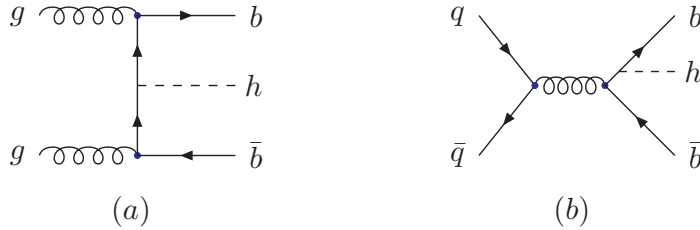


Figure 3: Representative diagrams for associated production of the Higgs boson and two high- p_T bottom quarks: (a) $gg \rightarrow b\bar{b}h$ (8 diagrams); (b) $q\bar{q} \rightarrow b\bar{b}h$ (2 diagrams).

In this paper we calculate the cross section for the associated production of the Higgs boson and a single bottom quark ($gb \rightarrow hb$) at next-to-leading order. We provide results for both the Tevatron and the LHC. The cross section for the subprocess $b\bar{b} \rightarrow h$ is already known at next-to-leading order [3, 18]. The cross section for the subprocess $gg, q\bar{q} \rightarrow b\bar{b}h$, which has two high- p_T bottom quarks, is known only at leading order, but the analogous subprocess $gg, q\bar{q} \rightarrow t\bar{t}h$ has been calculated at next-to-leading order [19, 20], so the next-to-leading-order result for $gg, q\bar{q} \rightarrow b\bar{b}h$ could be made available. Thus our calculation completes the set of next-to-leading-order cross sections for the subprocesses $b\bar{b} \rightarrow h$, $gb \rightarrow hb$, and $gg, q\bar{q} \rightarrow b\bar{b}h$.

In Section 2 we discuss the leading-order cross section for $gb \rightarrow hb$. In Section 3 we discuss the correction of order $1/\ln(m_h/m_b)$, due to initial gluons splitting into $b\bar{b}$ pairs. In Section 4 we discuss the correction of order α_S ; the virtual and real corrections are discussed separately. We present our numerical results in Section 5. Conclusions are drawn in Section 6.

Several appendices follow, in which the analytic results and some of the technical details are presented.

2 Leading order

The leading-order subprocess for Higgs-boson production in association with a single high- p_T bottom quark is shown in Fig. 2. Since the scale of the hard scattering is large compared with the b -quark mass, the b quark is regarded as part of the proton sea [21, 22, 23, 24]. However, unlike the light-quark sea, the b -quark sea is perturbatively calculable. This changes the way that one counts powers [3, 25]. If the scale of the hard scattering is μ , the b distribution function $b(x, \mu)$ is intrinsically of order $\alpha_S(\mu) \ln(\mu/m_b)$, in contrast with the light partons, which are of order unity. This captures the behavior of the b distribution function at low and high values of μ , and interpolates between them. As μ approaches m_b from above, $\ln(\mu/m_b)$ vanishes; this reflects the initial condition on the b distribution function, $b(x, m_b) = 0$. As μ becomes asymptotically large, $\alpha_S(\mu) \ln(\mu/m_b)$ approaches order unity,³ and the b distribution function becomes of the same order as the light partons.

With this counting, the leading-order subprocess $gb \rightarrow hb$ is of order $\alpha_S^2 \ln(m_h/m_b)$ (times the Yukawa coupling), where we have chosen the Higgs-boson mass as the relevant scale. The leading-order amplitude may be decomposed into a linear combination of two gauge-invariant subamplitudes,

$$\mathcal{A}_0^\mu = \mathcal{A}_A^\mu + \mathcal{A}_B^\mu . \quad (1)$$

These subamplitudes are gauge invariant in the sense that they each satisfy the Ward identity $p_{3\mu} \mathcal{A}_{A,B}^\mu = 0$, where $p_{3\mu}$ is the gluon four-momentum. They are related to the two independent helicity amplitudes for this subprocess. The explicit form of the subamplitudes and the helicity amplitudes are given in Appendix A.

The spin- and color-averaged cross section for $gb \rightarrow hb$ is

$$\frac{d\bar{\sigma}_{gb \rightarrow hb}}{dt} = -\frac{1}{s^2} \frac{\alpha_S(\mu)}{24} \left(\frac{y_b(\mu)}{\sqrt{2}} \right)^2 \frac{m_h^4 + u^2}{st} , \quad (2)$$

where s, t, u are the usual Mandelstam variables (the first and second diagrams in Fig. 2 have poles in the t and s channels, respectively), $\alpha_S(\mu)$ is the $\overline{\text{MS}}$ strong coupling, and $y_b(\mu)$ is the $\overline{\text{MS}}$ Yukawa coupling ($y_b(\mu)/\sqrt{2} = \overline{m}_b(\mu)/v$ in the standard model, where $\overline{m}_b(\mu)$ is the $\overline{\text{MS}}$ mass, and $v = (\sqrt{2}G_F)^{-1/2} \approx 246$ GeV). We choose the scale $\mu = m_h$ as our central value. It is important to use $\overline{m}_b(m_h)$ rather than the pole mass when evaluating the Yukawa coupling, as the latter is significantly greater than the former, and would yield an inflated cross section.⁴ The cross section for the charge-conjugate subprocess $\bar{g}\bar{b} \rightarrow h\bar{b}$ is identical. The cross section is also identical for the production of a pseudoscalar Higgs boson (A^0).

We neglect the b -quark mass in Eq. (2) and throughout, except in the evaluation of the Yukawa coupling. This corresponds to the simplified ACOT scheme [23, 24, 27]. The b -quark mass may be neglected, with no loss of accuracy, in any diagram in which the b quark is an

³This can be seen by recalling $\alpha_S(\mu) \approx 2\pi/(\beta_0 \ln(\mu/\Lambda_{QCD}))$.

⁴The evaluation of $\overline{m}_b(m_h)$ is detailed in Ref. [3]. We use $\overline{m}_b(\overline{m}_b) = 4.2$ GeV as the initial condition [26].

initial-state parton. Terms proportional to the b -quark mass enter only in the $1/\ln(m_h/m_b)$ correction. This is discussed at the end of the next section.

3 $1/\ln(m_h/m_b)$ correction

Consider the subprocess $gg, q\bar{q} \rightarrow b\bar{b}h$, shown in Fig. 3. It is of order α_S^2 (times the Yukawa coupling). Since the leading-order subprocess $gb \rightarrow hb$ is of order $\alpha_S^2 \ln(m_h/m_b)$, this subprocess is suppressed by $1/\ln(m_h/m_b)$ relative to the leading-order subprocess (for $m_h \gg m_b$) [3, 25].

The helicity amplitudes for this subprocess are given in Appendix B. Integration over the phase space of the final-state particles is divergent when the \bar{b} is collinear with an initial gluon,⁵ since we use $m_b = 0$. This collinear divergence is regulated using modern dimensional reduction (DR) [28], and absorbed into the b distribution function using a dipole-subtraction method [29] as formulated in Ref. [30].⁶ This subtraction, together with Gribov-Lipatov-Altarelli-Parisi evolution of the parton distribution functions, sums terms of order $\alpha_S^n \ln^n(m_h/m_b)$, to all orders in perturbation theory, into the b distribution function [21, 22, 23, 24]. This yields a well-behaved perturbation expansion in terms of the parameters $1/\ln(m_h/m_b)$ and α_S (the latter to be discuss in Section 4). Our final result is in the $\overline{\text{MS}}$ factorization scheme.

Some fraction of the events from this subprocess yield a final state with two b quarks at high p_T . In that case the contribution of this subprocess to the total cross section is enhanced, since either b can be tagged. If the b -tagging efficiency is ϵ_b , the probability of tagging one or more b quarks when both are at high p_T is $2\epsilon_b(1 - \epsilon_b) + \epsilon_b^2$. This results in an enhancement factor of $2 - \epsilon_b$ relative to subprocesses in which only one b quark is at high p_T . If the Higgs boson decays to $b\bar{b}$, the enhancement factor remains $2 - \epsilon_b$, if we demand three or more b tags and also demand that two of these tags come from the Higgs-boson decay products (so that two b -tagged jets reconstruct the Higgs-boson mass).

Since we neglect the b -quark mass throughout the calculation, we are making an approximation. To include the b -quark mass, one would calculate the diagrams of Fig. 3 with a finite quark mass [23, 24, 27]. This would introduce terms of order m_b^2/m_h^2 and m_b^2/p_T^2 . Hence the only approximation we are making by neglecting the b -quark mass throughout the calculation is of order $1/\ln(m_h/m_b) \times m_b^2/m_h^2$ and $1/\ln(m_h/m_b) \times m_b^2/p_T^2$.

4 α_S correction

In this section we discuss the genuine correction of order α_S . We divide it into two classes: virtual and real. Collinear divergences are isolated and absorbed into the parton distribution functions. Soft divergences cancel between the virtual and real corrections. Both types of divergences are regulated using modern dimensional reduction (DR) and are cancelled using a dipole-subtraction method, as in the previous section. Our final result is in the $\overline{\text{MS}}$ factorization scheme. The b -quark mass is neglected throughout this section; this introduces no approximation [23, 24, 27].

⁵This pertains only to $gg \rightarrow b\bar{b}h$, which makes a much larger contribution than $q\bar{q} \rightarrow b\bar{b}h$.

⁶See Ref. [31] for details on the implementation of this method.

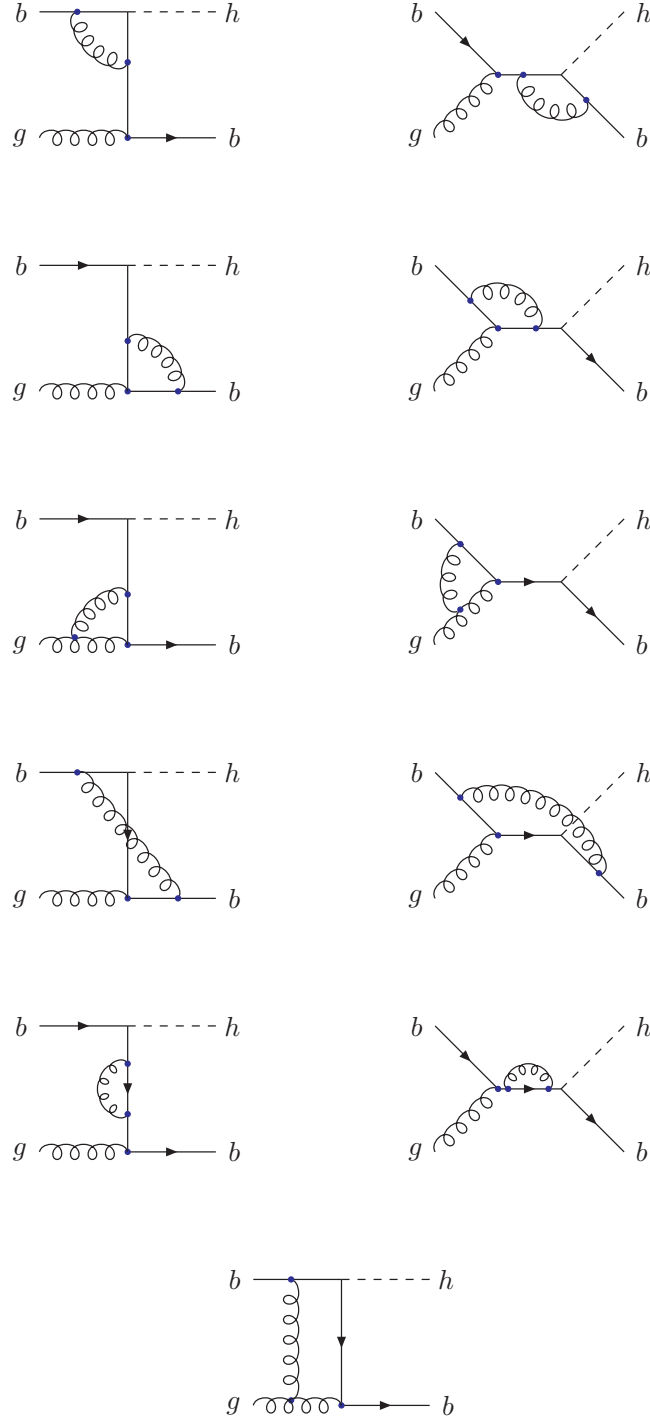


Figure 4: Virtual correction to $gb \rightarrow hb$. External-leg wavefunction renormalization diagrams (not shown) vanish in modern dimensional reduction for massless particles.

4.1 Virtual correction

The one-loop correction to the subprocess $gb \rightarrow hb$ is shown in Fig. 4. We calculate in $d = 4 - 2\epsilon$ dimensions, using modern dimensional reduction (DR). We also used conventional dimensional regularization (CDR) as a check on our calculation [32], as discussed in Appendix E. In DR, the result for the one-loop amplitude is

$$\begin{aligned} \mathcal{A}_1^\mu &= \mathcal{A}_0^\mu \frac{\alpha_S}{4\pi} \left[\frac{C_A}{2} \left(-2C(s) + D(s, u) - \frac{1}{2}D(s, t) + C'(u) \right) \right. \\ &\quad \left. + C_F (C(s) - D(s, u) - C'(t) - C'(u)) + (s \leftrightarrow t) \right] \\ &+ \mathcal{A}_B^\mu \frac{\alpha_S}{4\pi} (C_A - C_F), \end{aligned} \quad (3)$$

where the scalar loop integrals C, C', D are defined in Appendix C, and $C_F = (N_c^2 - 1)/2N_c = 4/3$, $C_A = N_c = 3$. The one-loop amplitude is proportional to the tree amplitude, \mathcal{A}_0^μ , except for the last term, which is proportional to one of the two gauge-invariant tree subamplitudes, \mathcal{A}_B^μ [Eq. (6)], times a finite constant. We checked that this amplitude has the structure of infrared (soft and collinear) divergences expected from the dipole-subtraction method (see Appendix E).

The above expression contains ultraviolet divergences. These are cancelled by the renormalization of the strong and Yukawa couplings, as discussed in Appendix E. The ultraviolet divergences are also regulated using modern dimensional reduction (DR). The renormalization of the Yukawa coupling with this regulator in the $\overline{\text{MS}}$ renormalization scheme is derived in Appendix D.

4.2 Real correction

The real correction of $\mathcal{O}(\alpha_S)$ has several contributions. Fig. 5(a) shows the contribution from real gluon emission, $gb \rightarrow gbh$; (b) shows the subprocesses $qb \rightarrow qbh$ and $\bar{q}b \rightarrow \bar{q}bh$; (c) shows the subprocess $bb \rightarrow bbh$; and (d) shows the subprocess $b\bar{b} \rightarrow b\bar{b}h$. Another real correction, $gg, q\bar{q} \rightarrow b\bar{b}h$, shown in Fig. 3, is of $\mathcal{O}(1/\ln(m_h/m_b))$; it is discussed in Section 3. The helicity amplitudes for these subprocesses are given in Appendix B.

The subprocess $bb \rightarrow bbh$ (and $b\bar{b} \rightarrow b\bar{b}h$) requires some additional consideration. Since there are two b quarks in the initial state, this subprocess is of order $\alpha_S^4 \ln^2(m_h/m_b)$, which is suppressed relative to the leading-order subprocess by $\alpha_S^2 \ln(m_h/m_b)$. Thus it is not truly a correction of order α_S . Nevertheless, it is a next-to-leading-order correction in powers of α_S and $1/\ln(m_h/m_b)$, so it is appropriate to include it in our calculation. Furthermore, this subprocess yields two b quarks in the final state. Thus, as discussed in Section 3, this subprocess is enhanced by a factor $2 - \epsilon_b$ when both b quarks are at high p_T . However, this contribution is less than one percent of the leading-order cross section, so this point is moot.

The subprocess $b\bar{b} \rightarrow b\bar{b}h$ has a contribution from the diagram shown in Fig. 5(d) in which a gluon splits into a final-state $b\bar{b}$ pair. Since we neglect the b mass throughout our calculation, this subprocess contains a divergence when the b and \bar{b} are collinear. In reality, the b -quark mass regulates this divergence. To approximate this effect, we restrict the $b\bar{b}$ invariant mass to be greater than $2m_b$. This correctly captures the dominant, logarithmically-

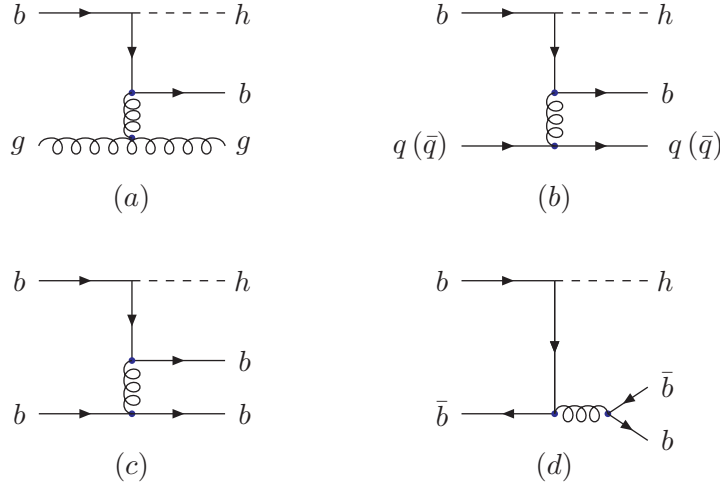


Figure 5: Representative diagrams for subprocesses contributing to the real correction to $gb \rightarrow hb$: (a) $gb \rightarrow gbh$ (8 diagrams); (b) $q(\bar{q})b \rightarrow q(\bar{q})bh$ (2 diagrams); (c) $bb \rightarrow bbh$ (8 diagrams); $b\bar{b} \rightarrow b\bar{b}h$ (8 diagrams).

enhanced term of order $\ln s/m_b^2$. Since this correction is less than one percent of the leading-order cross section, this approximation suffices.

5 Results

Figures 6 – 8 show the cross sections for associated production of the Higgs boson and a single bottom quark *vs.* the Higgs-boson mass at the Tevatron and the LHC. These cross sections pertain to both a scalar and a pseudoscalar Higgs boson. The Yukawa coupling is set to its standard-model value. At the Tevatron, the b jet⁷ is required to have a minimum p_T of 15 GeV and a rapidity of magnitude less than 2, such that it can be tagged by the silicon vertex detector; we refer to this as the tagging region. At the LHC the rapidity coverage is taken to be $|\eta(b)| < 2.5$. Two plots are given for the LHC, one with a minimum p_T of 15 GeV (appropriate for low-luminosity running) and one with 30 GeV (appropriate for high-luminosity running). Each figure has three curves. The curve labeled $\sigma_{\text{LO}}(1b)$ is the leading-order cross section, calculated with LO parton distribution functions (CTEQ5L [33]) and couplings evolved at LO, with the factorization and renormalization scales set to $\mu = m_h$.⁸ The notation indicates that there is only one b quark at high p_T . The curve labeled $\sigma_{\text{NLO}}(1b)$ is the next-to-leading-order cross section, calculated with NLO parton distribution functions (CTEQ5M1) and couplings evolved at NLO, with $\mu = m_h$. Only the subprocesses that yield a single b quark in the tagging region are included. Some of the NLO subprocesses yield two b quarks in the tagging region; this cross section is labeled $\sigma_{\text{NLO}}(2b)$ in the figures. This cross section is dominated by the subprocess $gg \rightarrow b\bar{b}h$, discussed in Section 3. The

⁷Partons within a cone of $\Delta R = 0.7$ are clustered into a single b jet.

⁸The evolution of $\alpha_S(\mu)$ uses the value of Λ_{QCD} corresponding to the parton distribution functions.

NLO cross section with one or more b tags is given by $\sigma_{\text{NLO}}(1b)\epsilon_b + \sigma_{\text{NLO}}(2b)(2\epsilon_b(1 - \epsilon_b) + \epsilon_b^2)$, where ϵ_b is the b -tagging efficiency. As is evident from the figures, the NLO cross section is dominated by the subprocesses with a single b quark in the tagging region.

The NLO correction ranges from 50 – 60% of the LO cross section at the Tevatron for $m_h = 100 - 200$ GeV. At the LHC, the correction ranges from 20 – 40% for $p_T > 15$ GeV, and 25 – 45% for $p_T > 30$ GeV, for $m_h = 120 - 500$ GeV.⁹ Most of the correction comes from the $\mathcal{O}(\alpha_S)$ contribution. The $\mathcal{O}(1/\ln(m_h/m_b))$ contribution is small, less than 10% of the LO cross section. Thus the terms we are neglecting by using $m_b = 0$ throughout the calculation, of order $1/\ln(m_h/m_b) \times m_b^2/m_h^2$ and $1/\ln(m_h/m_b) \times m_b^2/p_T^2$, are very small.

As discussed in the Introduction, recent analyses for the decay $h \rightarrow b\bar{b}$ use $gg, q\bar{q} \rightarrow h b\bar{b}$ as the Higgs-boson production subprocess, and demand a final state with four jets, with either at least three b tags, or with four b tags [5, 11, 14, 15, 16, 17]. The cross section with at least three b tags (two of which come from the decay products of the Higgs boson)¹⁰ is $\sigma_{\text{NLO}}(2b)(2\epsilon_b(1 - \epsilon_b) + \epsilon_b^2)$; with four b tags it is $\sigma_{\text{NLO}}(2b)\epsilon_b^2$. Both of these are an order of magnitude less than the cross section with three or more jets, with three or more b tags, given by $\sigma_{\text{NLO}}(1b)\epsilon_b + \sigma_{\text{NLO}}(2b)(2\epsilon_b(1 - \epsilon_b) + \epsilon_b^2)$. Thus our motivation for carrying out this calculation was well founded.

Similarly, the existing studies of $h \rightarrow \tau^+\tau^-, \mu^+\mu^-$ with at least one b tag use $gg, q\bar{q} \rightarrow b\bar{b}h$ as the Higgs-boson production subprocess [5, 10, 11]. One should instead use the NLO calculation of $gb \rightarrow hb$, since this is a much larger cross section.

The NLO calculation of the cross section for associated production of the Higgs boson and a single b quark gives a more accurate estimate of the cross section than the LO calculation. This is evidenced by the fact that the NLO calculation of the cross section is less sensitive to the choice of factorization and renormalization scales than the LO calculation. Typical examples are shown in Figs. 9 and 10, where we plot the LO and NLO cross section *vs.* the common factorization and renormalization scale μ , for $m_h = 120$ GeV at the Tevatron and the LHC (solid curves).¹¹ In Tables 1 and 2 we give the cross section evaluated at $\mu = m_h$ as the central value (these are the numbers plotted in Figs. 6 – 8), with uncertainties corresponding to $\mu = m_h/2$ (upper uncertainty) and $\mu = 2m_h$ (lower uncertainty). The scale dependence is significantly reduced when going from LO to NLO. Our NLO cross section can be used to normalize any future studies that make use of this production mechanism.

Also shown in Figs. 9 and 10 is the factorization-scale dependence of the cross section, with the renormalization scale fixed to $\mu = m_h$ (dashed curves). The factorization-scale dependence decreases at NLO, as expected. At the Tevatron, the factorization-scale dependence is negligible, even at LO. At the LHC, the factorization-scale dependence is greater than the dependence on the common factorization and renormalization scales. This indicates that there is compensation between the factorization and renormalization scales when the two are varied simultaneously.

The uncertainty in the choice of factorization and renormalization scales yields some uncertainty in the NLO cross section. In addition, there is an uncertainty in the cross section of about 10% due to the uncertainty in the Yukawa coupling ($\overline{m}_b(\overline{m}_b) = 4.2 \pm 0.2$),

⁹This is the size of the correction for $\mu = m_h$. The correction is less for smaller values of μ .

¹⁰A factor $BR(h \rightarrow b\bar{b})\epsilon_b^2$ is implicit in the following cross sections.

¹¹In this and the following figure, we take $\epsilon_b = 1$ when combining $\sigma_{\text{NLO}}(1b)$ and $\sigma_{\text{NLO}}(2b)$ to obtain the NLO cross section. However, the NLO cross section is dominated by $\sigma_{\text{NLO}}(1b)$ for any value of ϵ_b .

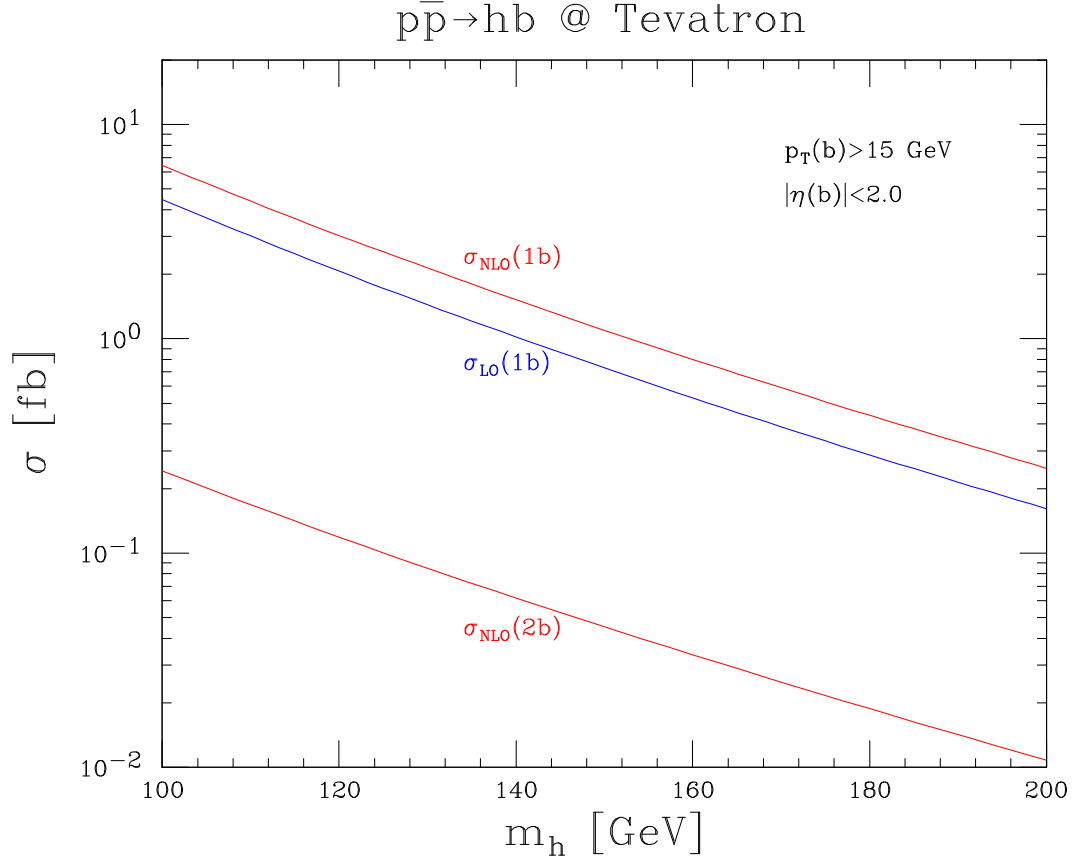


Figure 6: Cross section for the associated production of the Higgs boson and a single b quark at the Tevatron. The b quark is within the tagging region of the silicon vertex detector ($p_T > 15$ GeV, $|\eta| < 2$). The curve labeled $\sigma_{\text{LO}}(1b)$ is the leading-order cross section, evaluated with LO parton distribution functions (CTEQ5L) and couplings evolved at LO, evaluated at $\mu = m_h$. The notation indicates that there is only one b quark at high p_T . The curve labeled $\sigma_{\text{NLO}}(1b)$ is the next-to-leading-order cross section, evaluated with NLO parton distribution functions (CTEQ5M1) and couplings evolved at NLO, evaluated at $\mu = m_h$. Only the subprocesses that yield a single b quark in the tagging region are included. The cross section for NLO subprocesses that yield two b quarks in the tagging region is labeled $\sigma_{\text{NLO}}(2b)$.

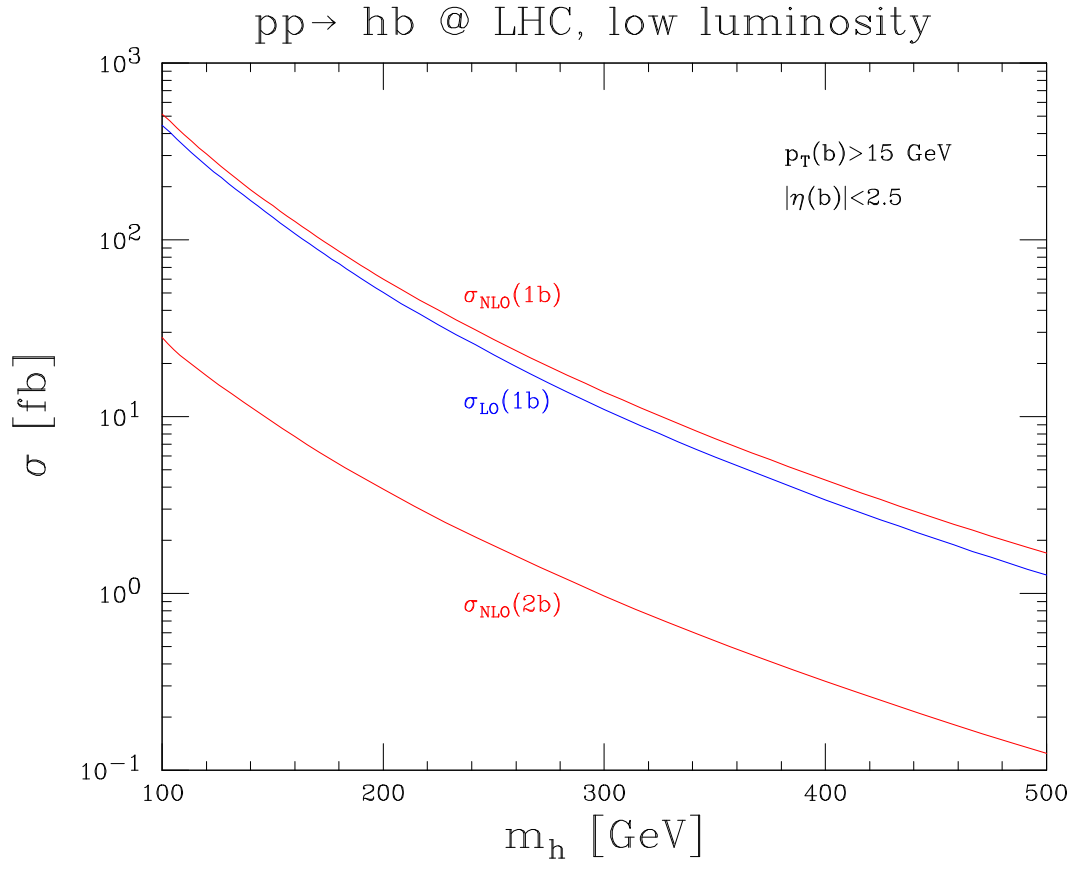


Figure 7: Same as Fig. 6, but at the LHC, and with a b -tagging region of $p_T > 15 \text{ GeV}$, $|\eta| < 2.5$.

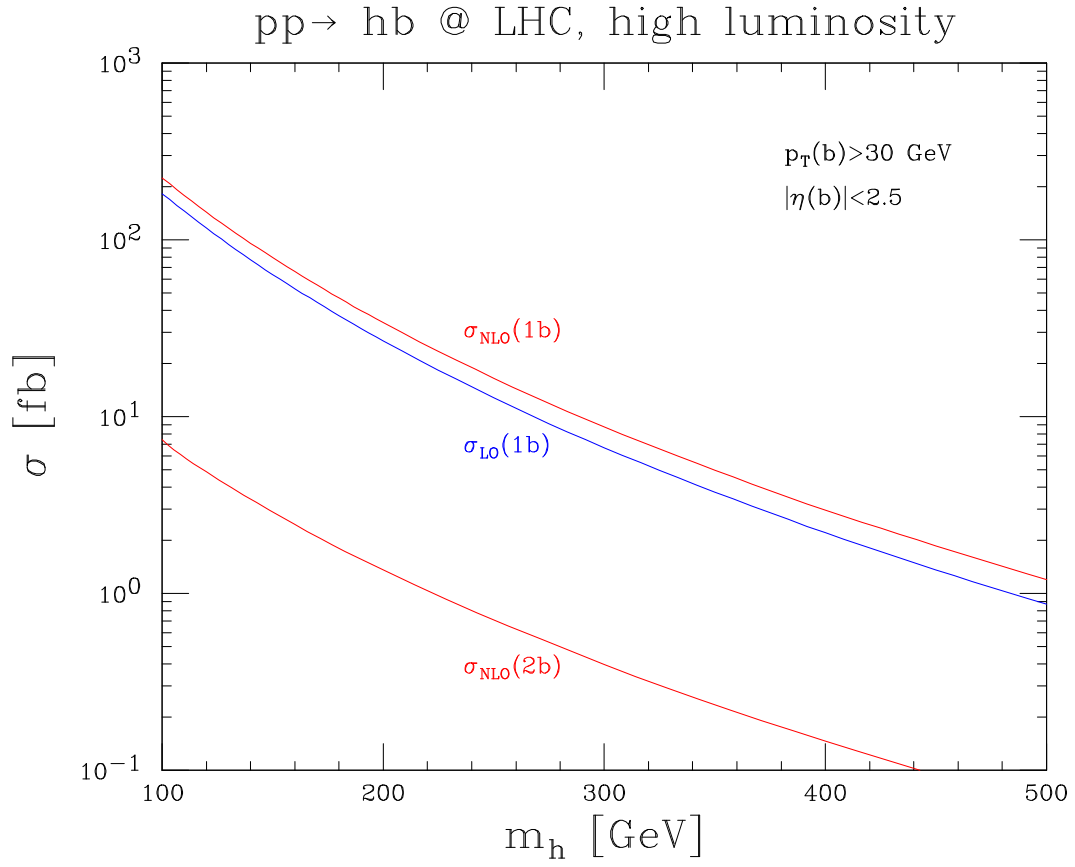


Figure 8: Same as Fig. 6, but at the LHC, and with a b -tagging region of $p_T > 30 \text{ GeV}$, $|\eta| < 2.5$.

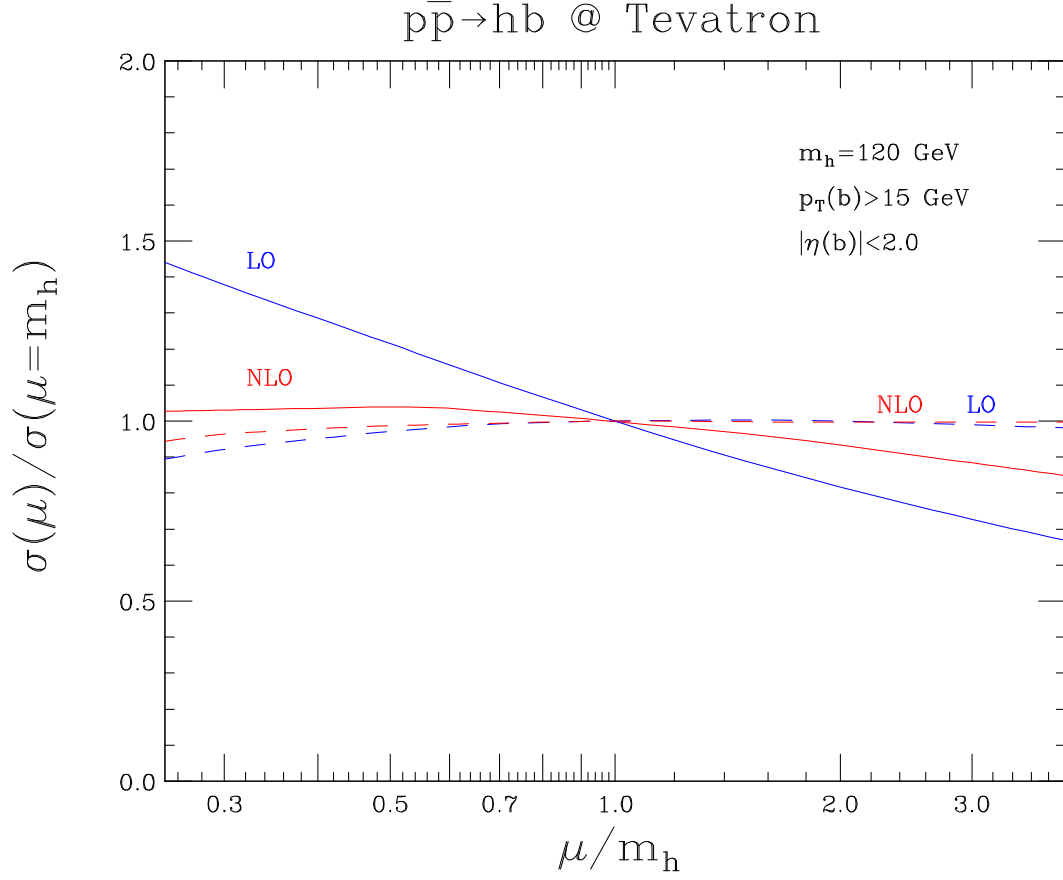


Figure 9: Cross section for the associated production of the Higgs boson and a single b quark *vs.* the common factorization and renormalization scale μ , for $m_h = 120$ GeV at the Tevatron (solid curves). The ratio of the cross section at scale μ to the cross section at scale $\mu = m_h$ is plotted *vs.* the ratio of the scales. The next-to-leading-order (NLO) cross section is less sensitive to the scale μ than the leading-order (LO) cross section. Also shown is the dependence on the factorization scale alone, with the renormalization scale fixed at $\mu = m_h$ (dashed curves).

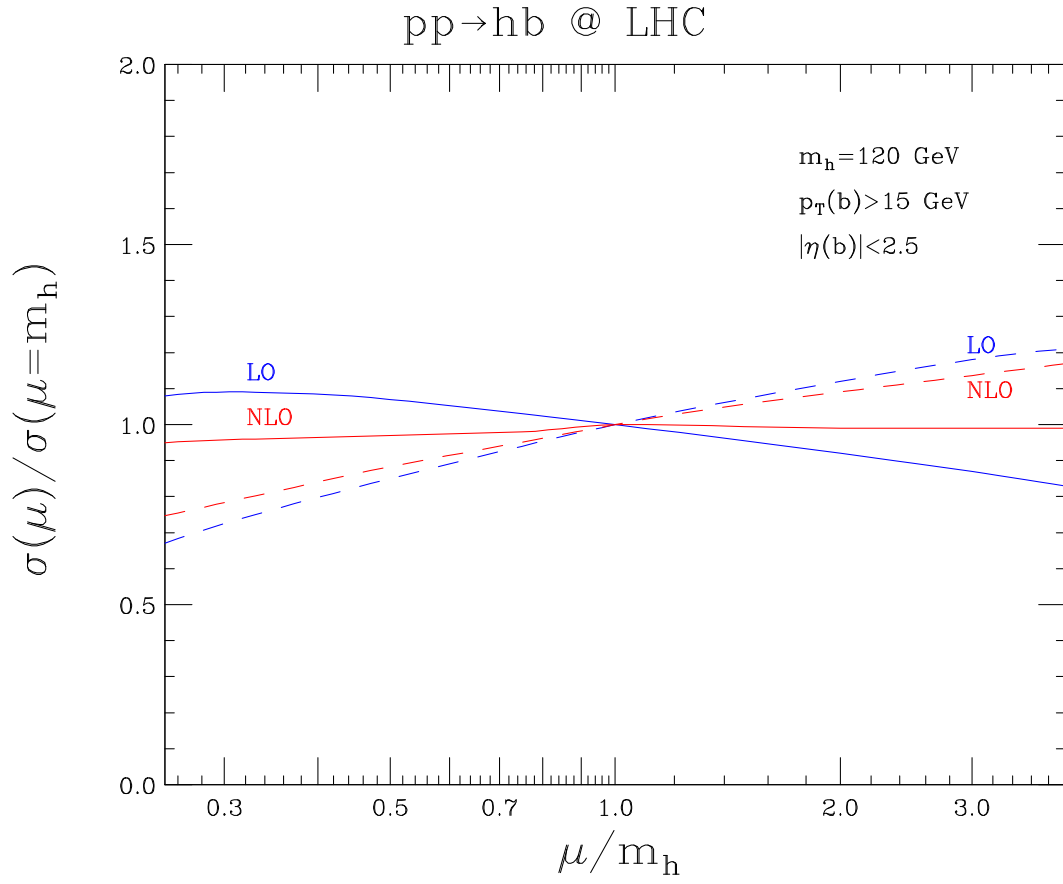


Figure 10: Same as Fig. 9, but at the LHC.

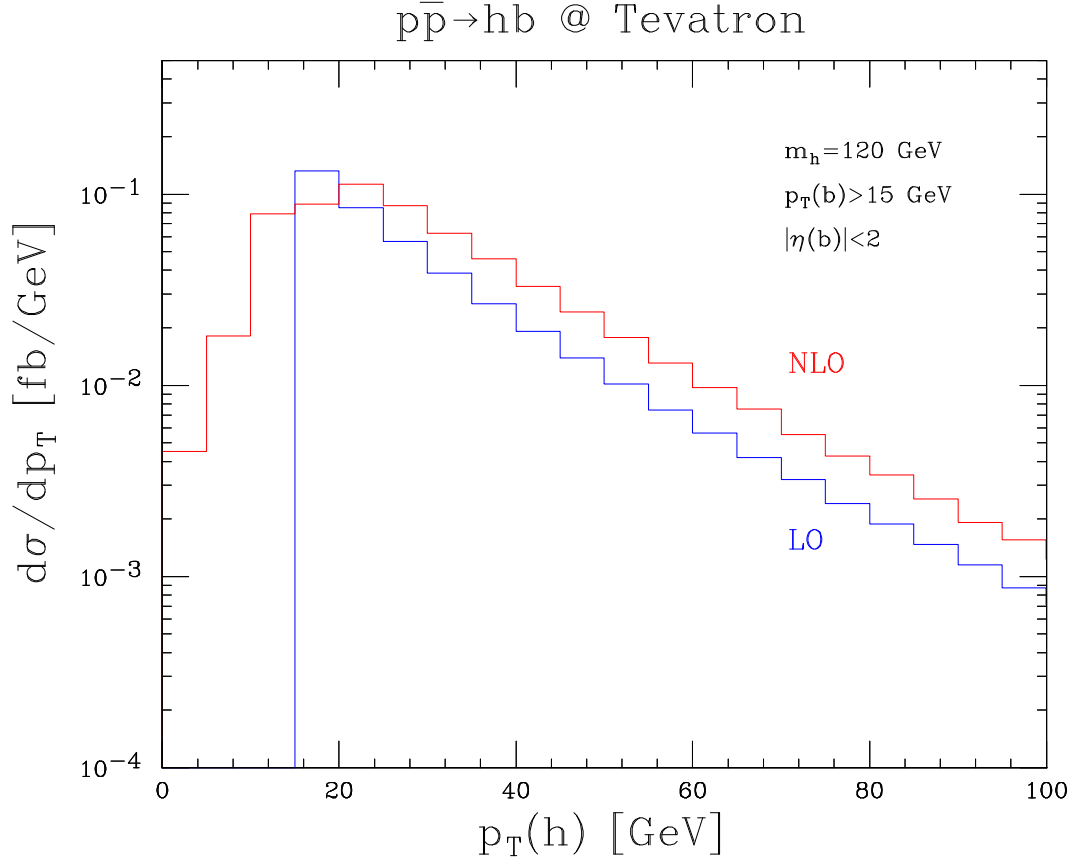


Figure 11: Higgs-boson p_T distribution for associated production of the Higgs boson and a single b quark, for $m_h = 120$ GeV at the Tevatron. At leading order (LO) the Higgs-boson p_T is balanced against that of the b quark, while at next-to-leading-order (NLO) it is balanced against that of the b quark and an additional parton.

Table 1: Cross sections (fb) for the associated production of the Higgs boson and a single b quark at the Tevatron. The central value corresponds to the choice of factorization and renormalization scale $\mu = m_h$; these values are plotted in Fig. 6. The uncertainty corresponds to varying the scale from $\mu = m_h/2$ to $\mu = 2m_h$. The b quark is within the tagging region of the silicon vertex detector ($p_T > 15$ GeV, $|\eta| < 2$). The column labeled $\sigma_{\text{LO}}(1b)$ is the leading-order cross section, evaluated with LO parton distribution functions (CTEQ5L) and couplings evolved at LO. The notation indicates that there is only one b quark at high p_T . The column labeled $\sigma_{\text{NLO}}(1b)$ is the next-to-leading-order cross section, evaluated with NLO parton distribution functions (CTEQ5M1) and couplings evolved at NLO. Only the subprocesses that yield a single b quark in the tagging region are included. The cross section for NLO subprocesses that yield two b quarks in the tagging region is labeled $\sigma_{\text{NLO}}(2b)$.

m_h (GeV)	$p\bar{p} @ \sqrt{s} = 2 \text{ TeV}$		
	$p_T(b) > 15 \text{ GeV}$		
	$\sigma_{\text{LO}}(1b)$	$\sigma_{\text{NLO}}(1b)$	$\sigma_{\text{NLO}}(2b)$
100	$4.49^{+19\%}_{-17\%}$	$6.45^{+0\%}_{-4\%}$	$0.24^{+62\%}_{-35\%}$
120	$2.06^{+22\%}_{-18\%}$	$3.03^{+2\%}_{-5\%}$	$0.12^{+62\%}_{-35\%}$
140	$1.02^{+23\%}_{-19\%}$	$1.52^{+3\%}_{-6\%}$	$0.062^{+62\%}_{-35\%}$
160	$0.529^{+25\%}_{-19\%}$	$0.80^{+2\%}_{-8\%}$	$0.034^{+63\%}_{-35\%}$
180	$0.287^{+26\%}_{-20\%}$	$0.44^{+3\%}_{-8\%}$	$0.019^{+63\%}_{-36\%}$
200	$0.162^{+27\%}_{-21\%}$	$0.25^{+4\%}_{-8\%}$	$0.011^{+63\%}_{-36\%}$

and of about 4% due to the uncertainty in the strong coupling [26]. The uncertainty in the gluon distribution function (which also reflects itself in the uncertainty in the b distribution function) is the source of another 10% uncertainty in the cross section [34].

Recall that it is only valid to use $gg, q\bar{q} \rightarrow b\bar{b}h$ as the production subprocess when both b quarks are at high p_T . To demonstrate this, we evaluated the cross section for the production of the Higgs boson and one high- p_T b quark using this subprocess by integrating over the momentum of the other b quark. For $m_h = 120$ GeV, this underestimates the NLO cross section by a factor of 4.6 at the Tevatron and 2.7 at the LHC. This factor is even larger for heavier Higgs bosons.

We also studied the kinematics of the Higgs boson at NLO *vs.* LO. The rapidity distribution of the Higgs boson remains almost unchanged. The p_T distribution of the Higgs boson does change at low p_T , as shown in Fig. 11. At LO, the p_T of the Higgs boson is balanced against that of the b quark, so the Higgs-boson p_T cannot be less than the minimum p_T of the b quark. This restriction is lifted at NLO, since the p_T of the Higgs boson is balanced against that of the b quark and an additional parton.

Table 2: Same as Table 1, but at the LHC. The left side of the table corresponds to a b -tagging region of $p_T > 15$ GeV, $|\eta| < 2.5$, appropriate for low-luminosity running. These cross sections are plotted in Fig. 7. The right side of the table corresponds to $p_T > 30$ GeV, $|\eta| < 2.5$, appropriate for high-luminosity running. These cross sections are plotted in Fig. 8.

m_h (GeV)	pp @ $\sqrt{s} = 14$ TeV					
	$p_T(b) > 15$ GeV			$p_T(b) > 30$ GeV		
	$\sigma_{\text{LO}}(1b)$	$\sigma_{\text{NLO}}(1b)$	$\sigma_{\text{NLO}}(2b)$	$\sigma_{\text{LO}}(1b)$	$\sigma_{\text{NLO}}(1b)$	$\sigma_{\text{NLO}}(2b)$
120	$269^{+5\%}_{-9\%}$	$305^{-1\%}_{+1\%}$	$17^{+38\%}_{-25\%}$	$117^{+7\%}_{-9\%}$	$143^{+1\%}_{-1\%}$	$4.9^{+40\%}_{-26\%}$
160	$108^{+10\%}_{-10\%}$	$127^{-2\%}_{+0\%}$	$7.7^{+37\%}_{-25\%}$	$52.8^{+10\%}_{-10\%}$	$66.2^{+1\%}_{-3\%}$	$2.5^{+40\%}_{-26\%}$
200	$49.9^{+13\%}_{-13\%}$	$60.1^{-1\%}_{-1\%}$	$3.9^{+39\%}_{-25\%}$	$26.8^{+12\%}_{-12\%}$	$34.0^{+1\%}_{-3\%}$	$1.4^{+40\%}_{-27\%}$
300	$11.0^{+15\%}_{-12\%}$	$13.8^{-1\%}_{-2\%}$	$1.0^{+40\%}_{-26\%}$	$6.67^{+14\%}_{-13\%}$	$8.8^{+2\%}_{-4\%}$	$0.40^{+41\%}_{-27\%}$
400	$3.39^{+16\%}_{-14\%}$	$4.37^{+0\%}_{-3\%}$	$0.32^{+40\%}_{-26\%}$	$2.21^{+16\%}_{-14\%}$	$2.96^{+2\%}_{-4\%}$	$0.15^{+41\%}_{-27\%}$
500	$1.27^{+18\%}_{-15\%}$	$1.69^{+0\%}_{-4\%}$	$0.12^{+42\%}_{-27\%}$	$0.872^{+18\%}_{-15\%}$	$1.20^{+2\%}_{-5\%}$	$0.062^{+41\%}_{-28\%}$

6 Conclusions

Previous studies of the associated production of the Higgs boson and a high- p_T bottom quark have used $gg, q\bar{q} \rightarrow b\bar{b}h$ as the production mechanism [1, 2, 4, 5, 10, 11, 12, 13, 14, 15, 16, 17], which is valid only if both b quarks are at high p_T . In this paper we have shown that the cross section for $gb \rightarrow hb$ [8, 9] is an order of magnitude larger than that of $gg, q\bar{q} \rightarrow b\bar{b}h$. This production mechanism improves the prospects for the discovery of a Higgs boson with enhanced coupling to the b quark. We evaluated the cross section for this subprocess at the Tevatron and the LHC at next-to-leading order in QCD. These cross sections can be used to normalize any future studies of this production mechanism. They pertain to both a scalar and a pseudoscalar Higgs boson. We have included $gb \rightarrow hb$ in the multi-purpose NLO Monte Carlo program MCFM [31, 35]. We encourage studies of the signal and backgrounds for associated production of the Higgs boson with a single high p_T bottom quark.

Acknowledgments

We are grateful for conversations and correspondence with C. Oleari and Z. Trócsányi. This work was supported in part by the U. S. Department of Energy under contracts Nos. DE-AC02-76CH03000 and DE-FG02-91ER40677.

Appendix A

In this Appendix we present explicit results for the leading-order subprocess $gb \rightarrow hb$. In order to be systematic, we give results for the (unphysical) crossed subprocess $0 \rightarrow \bar{b}bgh$, in which all particles are taken to be outgoing, as shown in Fig. 12. The amplitudes for the physical subprocesses $gb \rightarrow hb$ and $g\bar{b} \rightarrow h\bar{b}$ may then be obtained by crossing. The b -quark mass is neglected throughout. All expressions are presented in $d = 4 - 2\epsilon$ dimensions, using modern dimensional reduction.

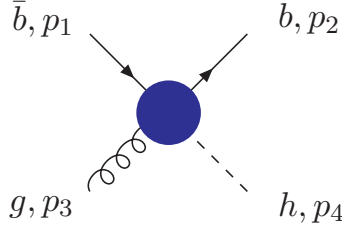


Figure 12: Four-momenta (all outgoing) of the particles for the (unphysical) subprocess $0 \rightarrow \bar{b}bgh$. The arrows indicate the flow of fermion number.

The amplitude for the leading-order subprocess $0 \rightarrow \bar{b}bgh$ may be written in terms of the four-momenta of the b , \bar{b} , and gluon. It is a linear combination of two gauge-invariant subamplitudes,

$$\mathcal{A}_0 \equiv \epsilon_\mu^{h_3*}(p_3)\mathcal{A}_0^\mu = \epsilon_\mu^{h_3*}(p_3)(\mathcal{A}_A^\mu + \mathcal{A}_B^\mu) \quad (4)$$

$$\mathcal{A}_A^\mu = i\mu^{2\epsilon}g_S\frac{y_b}{\sqrt{2}}\sqrt{2}T^a2\langle 2^{h_2}|1^{-h_2}\rangle\left(\frac{p_2^\mu}{s_{23}} - \frac{p_1^\mu}{s_{13}}\right) \quad (5)$$

$$\mathcal{A}_B^\mu = i\mu^{2\epsilon}g_S\frac{y_b}{\sqrt{2}}\sqrt{2}T^a\frac{m_h^2 - s_{12}}{s_{23}s_{13}}\langle 2^{h_2}|\gamma^\mu\hat{p}_3|1^{-h_2}\rangle, \quad (6)$$

where y_b is the $\overline{\text{MS}}$ Yukawa coupling ($y_b(\mu)/\sqrt{2} = \overline{m}_b(\mu)/v$ in the standard model, where $\overline{m}(\mu)$ is the $\overline{\text{MS}}$ mass and $v = (\sqrt{2}G_F)^{-1/2} \approx 246$ GeV), T^a are the fundamental-representation matrices of $SU(3)$ ($\text{Tr } T^a T^b = \delta^{ab}/2$), $s_{ij} \equiv (p_i + p_j)^2$, $\hat{p}_3 \equiv \gamma_\mu p_3^\mu$, $|1^\pm\rangle \equiv v^\mp(p_1)$, $\langle 2^\pm| \equiv \overline{u}^\pm(p_2)$, μ is the 't Hooft mass (introduced such that the renormalized couplings are dimensionless in d dimensions), h_2 denotes the helicity of the b quark (the \bar{b} has the same helicity in the massless approximation), and h_3 denotes the helicity of the gluon. The subamplitudes are gauge invariant in the sense that they each satisfy the Ward identity $p_{3\mu}\mathcal{A}_{A,B}^\mu = 0$.

One may also describe this subprocess in terms of helicity amplitudes. We define helicity amplitudes, A , with the overall factors of the coupling constants removed,

$$\mathcal{A}_0(1_b^{h_1}, 2_b^{h_2}, 3_g^{h_3}) = \mu^{2\epsilon}g_S\frac{y_b}{\sqrt{2}}\sqrt{2}T^a A(1_b^{h_1}, 2_b^{h_2}, 3_g^{h_3}), \quad (7)$$

where the Higgs-boson four-momentum is tacit. There are two independent helicity amplitudes,

$$A(1_b^+, 2_b^+, 3_g^+) = i\frac{m_h^2}{\langle 13\rangle\langle 23\rangle} \quad (8)$$

$$A(1_b^+, 2_b^+, 3_g^-) = i \frac{[12]^2}{[13][23]}, \quad (9)$$

using the spinor inner-product notation as reviewed in Ref. [36]. The helicity-reversed amplitudes are equal to these (times -1 if the Higgs boson is a pseudoscalar), by parity. The helicity amplitudes are related to the amplitudes \mathcal{A}_A^μ and \mathcal{A}_B^μ above by

$$\epsilon_\mu^{\pm*}(p_3) \mathcal{A}_A^\mu = \mathcal{A}_0(1_b^\mp, 2_b^\mp, 3_g^\pm) \quad (10)$$

$$\epsilon_\mu^{\pm*}(p_3) \mathcal{A}_B^\mu = \mathcal{A}_0(1_b^\pm, 2_b^\pm, 3_g^\pm). \quad (11)$$

Squaring the amplitude and summing over colors and helicities gives

$$\sum_{\text{col, hel}} |\mathcal{A}_0|^2 = \text{sgn}(s_{12}) 16 \mu^{4\epsilon} g_S^2 \left(\frac{y_b}{\sqrt{2}} \right)^2 \frac{m_h^4 + s_{12}^2}{s_{13} s_{23}}. \quad (12)$$

The spin- and color-averaged cross section for the physical subprocess $gb \rightarrow hb$, Eq. (2), is then obtained from the above by crossing ($s_{12} \rightarrow u$, $s_{13} \rightarrow s$, $s_{23} \rightarrow t$).

In the dipole-subtraction method, the tensor

$$\begin{aligned} \sum_{\text{col}, h_2=\pm 1} \mathcal{A}_0^\mu \mathcal{A}_0^{\nu*} = & 8 \mu^{4\epsilon} g_S^2 \left(\frac{y_b}{\sqrt{2}} \right)^2 \left[-g^{\mu\nu} \frac{(s_{13} + s_{23})^2}{s_{13} s_{23}} + 4 m_h^2 \left(\frac{p_2^\mu}{s_{23}} - \frac{p_1^\mu}{s_{13}} \right) \left(\frac{p_2^\nu}{s_{23}} - \frac{p_1^\nu}{s_{13}} \right) - \right. \\ & \left. 4 \frac{s_{12}}{s_{13} s_{23}} p_3^\mu p_3^\nu - 2 \frac{s_{12} s_{13} - m_h^2 s_{23}}{s_{13}^2 s_{23}} (p_3^\mu p_1^\nu + p_3^\nu p_1^\mu) - 2 \frac{s_{12} s_{23} - m_h^2 s_{13}}{s_{13} s_{23}^2} (p_3^\mu p_2^\nu + p_3^\nu p_2^\mu) \right] \end{aligned} \quad (13)$$

is also needed.

Appendix B

We present the helicity amplitudes for the $2 \rightarrow 3$ subprocesses shown in Figs. 3 and 5. All amplitudes are calculated in $d = 4$ dimensions. The amplitudes in $d = 4 - 2\epsilon$ dimensions using modern dimensional reduction may be obtained via $g_S \rightarrow g_S \mu^\epsilon$, $y_b \rightarrow y_b \mu^\epsilon$. The calculations were checked with the code MADGRAPH [37].

The subprocesses shown in Figs. 3(a) and 5(a) may be obtained from the helicity amplitudes for the unphysical subprocess $0 \rightarrow \bar{b} b g g h$. These helicity amplitudes may be written as

$$\mathcal{A}(1_b^{h_1}, 2_b^{h_2}, 3_g^{h_3}, 4_g^{h_4}) = (g_S \sqrt{2})^2 \frac{y_b}{\sqrt{2}} \left(\frac{\{T^a, T^b\}}{2} A_s + \frac{[T^a, T^b]}{2} A_a \right), \quad (14)$$

where A_s and A_a are the symmetric and antisymmetric combination of color-ordered amplitudes. The three independent helicity configurations are given by $(s_{ijk} \equiv (p_i + p_j + p_k)^2)$

$$A_s(1_b^+, 2_b^+; 3_g^+, 4_g^+) = -i \frac{m_h^2 \langle 12 \rangle}{\langle 13 \rangle \langle 14 \rangle \langle 23 \rangle \langle 24 \rangle} \quad (15)$$

$$A_a(1_b^+, 2_b^+; 3_g^+, 4_g^+) = i \frac{m_h^2}{\langle 34 \rangle} \left(\frac{1}{\langle 13 \rangle \langle 24 \rangle} + \frac{1}{\langle 14 \rangle \langle 23 \rangle} \right) \quad (16)$$

$$A_s(1_b^+, 2_b^+; 3_g^-, 4_g^-) = i \frac{[12]^3}{[13][14][23][24]} \quad (17)$$

$$A_a(1_b^+, 2_b^+; 3_g^-, 4_g^-) = -i \frac{[12]^2}{[34]} \left(\frac{1}{[13][24]} + \frac{1}{[14][23]} \right) \quad (18)$$

$$A_s(1_b^+, 2_b^+; 3_g^+, 4_g^-) = i \left(\frac{[12] s_{123}}{\langle 13 \rangle \langle 23 \rangle [14][24]} + \frac{[13] (\langle 14 \rangle [12] - \langle 34 \rangle [23])}{\langle 13 \rangle [14] s_{134}} + \frac{(\langle 24 \rangle [12] + \langle 34 \rangle [13]) [23]}{\langle 23 \rangle [24] s_{234}} \right) \quad (19)$$

$$A_a(1_b^+, 2_b^+; 3_g^+, 4_g^-) = i \left[\frac{\langle 34 \rangle [23] - \langle 14 \rangle [12]}{\langle 13 \rangle s_{34}} \left(-\frac{[23]}{[24]} + \frac{(-s_{13} + s_{14}) [13]}{[14] s_{134}} \right) - \frac{\langle 24 \rangle [12] + \langle 34 \rangle [13]}{\langle 23 \rangle s_{34}} \left(\frac{[13]}{[14]} + \frac{(s_{23} - s_{24}) [23]}{[24] s_{234}} \right) \right] . \quad (20)$$

Since these are not color-ordered amplitudes, the order of the gluons in the arguments of the functions A_s and A_a is irrelevant. Squaring and summing over colors gives

$$\sum_{\text{col}} |\mathcal{A}(1_b^{h_1}, 2_b^{h_2}, 3_g^{h_3}, 4_g^{h_4})|^2 = g_S^4 \left(\frac{y_b}{\sqrt{2}} \right)^2 \frac{N_c^2 - 1}{2} \left(\frac{N_c^2 - 2}{N_c} |A_s|^2 + N_c |A_a|^2 \right) . \quad (21)$$

The four-quark subprocess of Figs. 3(b) and 5(b) may be obtained from the helicity amplitudes for the unphysical subprocess $0 \rightarrow \bar{b}b\bar{q}qh$,

$$\mathcal{A}(1_b^{h_1}, 2_b^{h_2}, 3_q^{h_3}, 4_q^{h_4}) = (g_S \sqrt{2})^2 \frac{y_b}{\sqrt{2}} \frac{1}{2} \left(\delta_{i_4}^{\bar{i}_1} \delta_{i_2}^{\bar{i}_3} - \frac{1}{N_c} \delta_{i_2}^{\bar{i}_1} \delta_{i_4}^{\bar{i}_3} \right) A . \quad (22)$$

The two independent helicity configurations are given by

$$A(1_b^+, 2_b^+, 3_q^+, 4_q^-) = f(1, 2, 3, 4) + f(2, 1, 3, 4) \quad (23)$$

$$A(1_b^+, 2_b^+, 3_q^-, 4_q^+) = f(1, 2, 4, 3) + f(2, 1, 4, 3) , \quad (24)$$

where

$$f(1, 2, 3, 4) = i \frac{[13] (\langle 14 \rangle [12] - \langle 34 \rangle [23])}{s_{34} s_{134}} . \quad (25)$$

Squaring and summing over colors gives

$$\sum_{\text{col}} |\mathcal{A}(1_b^{h_1}, 2_b^{h_2}, 3_q^{h_3}, 4_q^{h_4})|^2 = g_S^4 \left(\frac{y_b}{\sqrt{2}} \right)^2 (N_c^2 - 1) |A|^2 . \quad (26)$$

The four- b -quark subprocesses in Figs. 5(c) and (d) may be obtained from the helicity amplitudes for the unphysical subprocess $0 \rightarrow \bar{b}b\bar{b}bh$. These helicity amplitudes may be obtained from the four-quark amplitudes above by subtracting a term with one pair of the identical quarks exchanged,

$$\mathcal{A}(1_b^{h_1}, 2_b^{h_2}, 3_b^{h_3}, 4_b^{h_4}) = (g_S \sqrt{2})^2 \frac{y_b}{\sqrt{2}} \frac{1}{2} \left[\left(\delta_{i_4}^{\bar{i}_1} \delta_{i_2}^{\bar{i}_3} - \frac{1}{N_c} \delta_{i_2}^{\bar{i}_1} \delta_{i_4}^{\bar{i}_3} \right) A - \left(\delta_{i_2}^{\bar{i}_1} \delta_{i_4}^{\bar{i}_3} - \frac{1}{N_c} \delta_{i_4}^{\bar{i}_1} \delta_{i_2}^{\bar{i}_3} \right) A^{\text{ex}} \right] , \quad (27)$$

where

$$A = A(1_b^{h_1}, 2_b^{h_2}, 3_b^{h_3}, 4_b^{h_4}) \quad (28)$$

$$A^{\text{ex}} = \delta_{h_2 h_4} A(1_b^{h_1}, 4_b^{h_4}, 3_b^{h_3}, 2_b^{h_2}) + \delta_{h_1 h_3} A(3_b^{h_3}, 2_b^{h_2}, 1_b^{h_1}, 4_b^{h_4}) . \quad (29)$$

The four independent helicity configurations are given by

$$A(1_b^+, 2_b^+, 3_b^+, 4_b^-) = f(1, 2, 3, 4) + f(2, 1, 3, 4) \quad (30)$$

$$A(1_b^+, 2_b^+, 3_b^-, 4_b^+) = f(1, 2, 4, 3) + f(2, 1, 4, 3) \quad (31)$$

$$A(1_b^+, 2_b^-, 3_b^+, 4_b^+) = f(3, 4, 1, 2) + f(4, 3, 1, 2) \quad (32)$$

$$A(1_b^-, 2_b^+, 3_b^+, 4_b^+) = f(3, 4, 2, 1) + f(4, 3, 2, 1) . \quad (33)$$

Squaring and summing over colors gives

$$\sum_{\text{col}} |\mathcal{A}(1_b^{h_1}, 2_b^{h_2}, 3_q^{h_3}, 4_q^{h_4})|^2 = g_S^4 \left(\frac{y_b}{\sqrt{2}} \right)^2 (N_c^2 - 1) \left(|A|^2 + |A^{\text{ex}}|^2 + \frac{2}{N_c} \text{Re}(A^{\text{ex}} A^*) \right) . \quad (34)$$

Appendix C

In this appendix we list the scalar integrals which result from the Passarino-Veltman tensor reduction of the one-loop diagrams of Fig. 4, as given in Eq. (3). We define ($d = 4 - 2\epsilon$)

$$B_0(p_1^2; m_0^2, m_1^2) \equiv \mu^{2\epsilon} \int \frac{d^d k}{(2\pi)^d} \frac{1}{[k^2 - m_0^2][(k + p_1)^2 - m_1^2]} \quad (35)$$

$$C_0(p_1^2, p_2^2, p_{12}^2; m_0^2, m_1^2, m_2^2) \equiv \mu^{2\epsilon} \int \frac{d^d k}{(2\pi)^d} \frac{1}{[k^2 - m_0^2][(k + p_1)^2 - m_1^2][(k + p_1 + p_2)^2 - m_2^2]} \quad (36)$$

$$D_0(p_1^2, p_2^2, p_3^2, p_4^2, p_{12}^2, p_{23}^2; m_0^2, m_1^2, m_2^2, m_3^2) \equiv \mu^{2\epsilon} \int \frac{d^d k}{(2\pi)^d} \frac{1}{[k^2 - m_0^2][(k + p_1)^2 - m_1^2][(k + p_1 + p_2)^2 - m_2^2][(k + p_1 + p_2 + p_3)^2 - m_3^2]} \quad (37)$$

where $p_{ij}^2 = (p_i + p_j)^2$, and

$$c_\Gamma \equiv (4\pi)^\epsilon \frac{\Gamma(1 + \epsilon)\Gamma^2(1 - \epsilon)}{\Gamma(1 - 2\epsilon)} . \quad (38)$$

The scalar integrals needed are (s and t are generic invariants here)

$$B_0(0; 0, 0) = 0 \quad (39)$$

$$B_0(s; 0, 0) = \frac{ic_\Gamma}{16\pi^2} \left(\frac{1}{\epsilon} + 2 - \ln \frac{-s}{\mu^2} \right) \quad s < 0 \quad (40)$$

$$C_0(0, 0, s; 0, 0, 0) \equiv \frac{iC(s)}{s} = \frac{ic_\Gamma}{16\pi^2} \frac{1}{s} \left(\frac{1}{\epsilon^2} - \frac{1}{\epsilon} \ln \frac{-s}{\mu^2} + \frac{1}{2} \ln^2 \frac{-s}{\mu^2} \right) \quad s < 0 \quad (41)$$

$$\begin{aligned}
C_0(m_h^2, 0, s; 0, 0, 0) &\equiv \frac{iC'(s)}{m_h^2 - s} \\
&= \frac{ic_\Gamma}{16\pi^2} \frac{1}{m_h^2 - s} \left[\frac{1}{\epsilon} \ln \frac{-s}{-m_h^2} - \frac{1}{2} \left(\ln^2 \frac{-s}{\mu^2} - \ln^2 \frac{-m_h^2}{\mu^2} \right) \right] \\
&\quad s, m_h^2 < 0
\end{aligned} \tag{42}$$

$$\begin{aligned}
D_0(0, 0, 0, m_h^2, s, t; 0, 0, 0, 0) &\equiv \frac{iD(s, t)}{st} \\
&= \frac{ic_\Gamma}{16\pi^2} \left(\frac{\mu^2}{-m_h^2} \right)^\epsilon \frac{2}{st} \left[\frac{1}{\epsilon^2} - \frac{1}{\epsilon} \left(\ln \frac{-s}{-m_h^2} + \ln \frac{-t}{-m_h^2} \right) \right. \\
&\quad \left. + \frac{1}{2} \left(\ln^2 \frac{-s}{-m_h^2} + \ln^2 \frac{-t}{-m_h^2} \right) + \text{R} \left(\frac{-s}{-m_h^2}, \frac{-t}{-m_h^2} \right) \right] \\
&\quad m_h^2 < s, t < 0
\end{aligned} \tag{43}$$

$$\text{R}(x, y) = \ln x \ln y - \ln x \ln(1-x) - \ln y \ln(1-y) + \frac{\pi^2}{6} - \text{Li}_2(x) - \text{Li}_2(y) . \tag{44}$$

The analytic continuation of the above results to the physical region is accomplished through the use of

$$\ln(-s - i\eta) = \ln |s| - i\pi\Theta(s) , \tag{45}$$

where s is a generic invariant (including m_h^2) and η is a small positive number and, for the dilogarithms with arguments greater than unity, by means of

$$\text{Re} [\text{Li}_2(x)] = -\text{Li}_2 \left(\frac{1}{x} \right) + \frac{\pi^2}{3} - \frac{1}{2} \ln^2 x . \tag{46}$$

Appendix D

In this appendix we derive the QCD counterterm for the Yukawa coupling in the $\overline{\text{MS}}$ renormalization scheme [38]. We consider two different regularization schemes (RS): conventional dimensional regularization (CDR) and modern dimensional reduction (DR).

The Yukawa coupling and the quark mass arise from a common term in the Lagrangian,

$$\mathcal{L} = -\frac{y_0}{\sqrt{2}} \overline{Q} Q (h + v) , \tag{47}$$

where y_0 is the bare Yukawa coupling, h is the physical Higgs-boson field, and $v = (\sqrt{2}G_F)^{-1/2} \approx 246$ GeV is the vacuum-expectation value of the Higgs-doublet field. It is evident from Eq. (47) that the bare quark mass is related to the bare Yukawa coupling by $m_0 = y_0 v / \sqrt{2}$.

The quark mass and Yukawa coupling receive corrections at one loop in QCD. We express the bare parameters in terms of the $\overline{\text{MS}}$ values and a counterterm,

$$y_0 = \mu^\epsilon y (1 + \delta y_{\text{RS}}) \tag{48}$$

$$m_0 = \overline{m} + \delta m_{\text{RS}} , \tag{49}$$

where the subscript on the counterterm indicates that it depends on the regularization scheme (RS). The parameter μ is the 't Hooft mass, introduced to keep the renormalized Yukawa coupling dimensionless in $d = 4 - 2\epsilon$ dimensions. The Higgs vacuum-expectation value does not receive a correction at one loop in QCD. From the above equations and the relation $m_0 = y_0 v / \sqrt{2}$ we find that the mass and Yukawa-coupling counterterms are related by $\delta y_{\text{RS}} = \delta m_{\text{RS}} / \overline{m}$. Thus we may obtain the Yukawa-coupling counterterm from the mass counterterm.

The one-loop quark propagator is given by

$$\frac{i}{\hat{p} - m_0 + \Sigma_{\text{RS}}(\hat{p})} = \frac{i}{\hat{p} - \overline{m} - \delta m_{\text{RS}} + \Sigma_{\text{RS}}(\hat{p})} , \quad (50)$$

where $i\Sigma_{\text{RS}}(\hat{p})$ is the one-loop quark self energy. Since it is ultraviolet divergent, it depends on the regularization scheme. The position of the pole in the propagator at one loop is¹²

$$m_{\text{pole}} = \overline{m} + \delta m_{\text{RS}} - \Sigma_{\text{RS}}(m) . \quad (51)$$

The $\overline{\text{MS}}$ mass is defined via

$$\delta m_{\text{CDR}} = \Sigma(m)|_{\text{div}} , \quad (52)$$

where $\Sigma(m)|_{\text{div}}$ is the divergent part, proportional to c_Γ/ϵ , of the quark self energy (which is the same in CDR and DR). Since the pole mass is a physical quantity,¹³ independent of the regularization scheme, Eqs. (51) and (52) yield

$$\delta m_{\text{DR}} = \Sigma(m)|_{\text{div}} + \Sigma_{\text{DR}}(m) - \Sigma_{\text{CDR}}(m) . \quad (53)$$

The one-loop quark self energy (in 't Hooft-Feynman gauge) is

$$\begin{aligned} i\Sigma_{\text{RS}}(\hat{p}) &= \int \frac{d^d k}{(2\pi)^d} (ig_S \mu^\epsilon \gamma^\nu T^a) \frac{i}{\hat{p} + \hat{k} - m} (ig_S \mu^\epsilon \gamma^\mu T^a) \frac{-ig_{\mu\nu}}{k^2} \\ &= -g_S^2 C_F \begin{cases} [(-2 + 2\epsilon)\hat{p} + (4 - 2\epsilon)m] B(p^2) + (-2 + 2\epsilon)\hat{p} A(p^2) & \text{in CDR} \\ (-2\hat{p} + 4m) B(p^2) - 2\hat{p} A(p^2) & \text{in DR} \end{cases} \end{aligned} \quad (54)$$

where $C_F = (N_c^2 - 1)/2N_c = 4/3$ and

$$A(p^2) p^\alpha \equiv \mu^{2\epsilon} \int \frac{d^d k}{(2\pi)^d} \frac{k^\alpha}{k^2 [(p+k)^2 - m^2]} \quad (55)$$

$$B(p^2) = B_0(p^2; 0, m^2) . \quad (56)$$

Using

$$A(m^2) = -\frac{i}{16\pi^2} \left(\frac{\mu^2}{m^2} \right)^\epsilon c_\Gamma \left(\frac{1}{2\epsilon} + \frac{1}{2} \right) \quad (57)$$

$$B(m^2) = \frac{i}{16\pi^2} \left(\frac{\mu^2}{m^2} \right)^\epsilon c_\Gamma \left(\frac{1}{\epsilon} + 2 \right) , \quad (58)$$

¹²At one loop, the mass m in the argument of the quark self energy may be regarded as the pole mass or the $\overline{\text{MS}}$ mass.

¹³The quark pole mass is a physical quantity within perturbation theory, which suffices for our purposes. However, it is unphysical once nonperturbative QCD is taken into account [39, 40].

gives

$$\Sigma_{\text{RS}}(m) = -\frac{\alpha_S}{4\pi} C_F \left(\frac{\mu^2}{m^2} \right)^\epsilon c_\Gamma \left[\frac{3}{\epsilon} + 4 + \delta_{\text{RS}} \right] m, \quad (59)$$

where $\delta_{\text{CDR}} = 0$ and $\delta_{\text{DR}} = 1$. The counterterm is then obtained from Eqs. (52) and (53),

$$\delta m_{\text{RS}} = -\frac{\alpha_S}{4\pi} C_F c_\Gamma \left[\frac{3}{\epsilon} + \delta_{\text{RS}} \right] m. \quad (60)$$

Using $\delta y_{\text{RS}} = \delta m_{\text{RS}}/\overline{m}$ then gives

$$\delta y_{\text{RS}} = -\frac{\alpha_S}{4\pi} C_F c_\Gamma \left[\frac{3}{\epsilon} + \delta_{\text{RS}} \right]. \quad (61)$$

This result is independent of the gauge chosen.

The $\overline{\text{MS}}$ counterterm for the strong coupling, $g_S^0 = \mu^\epsilon g_S(1 + \delta g_S^{\text{RS}})$, analogous to Eq. (61), is [28]

$$\delta g_S^{\text{RS}} = \frac{\alpha_S}{4\pi} c_\Gamma \left[-\frac{b_0}{\epsilon} + \frac{C_A}{6} \delta_{\text{RS}} \right], \quad (62)$$

where $b_0 = \beta_0/2 = (11/6)C_A - (2/3)T_F n_f$, $C_A = N_c = 3$, $T_F = 1/2$, n_f is the number of light quarks, and $\delta_{\text{CDR}} = 0$, $\delta_{\text{DR}} = 1$.

The relation between the pole mass and $\overline{\text{MS}}$ mass may also be obtained from Eqs. (51), (52), and (59),

$$m_{\text{pole}} = \overline{m}(\mu) \left[1 + \frac{\alpha_S}{4\pi} C_F \left(4 + 3 \ln \frac{\mu^2}{m^2} \right) \right]. \quad (63)$$

Appendix E

In this appendix we discuss two of the checks performed on our calculation of the virtual correction presented in Section 4.1 and Appendix C. We checked that the structure of the infrared (soft and collinear) divergences is as expected from the dipole-subtraction method [30]. We also performed the calculation in both conventional dimensional regularization (CDR) and modern dimensional reduction (DR) and verified the scheme independence of our results.

The structure of the divergences for $gb \rightarrow hb$ at one loop is

$$\begin{aligned} 2\text{Re}(\mathcal{A}_1 \mathcal{A}_0^*)|_{\text{div}} &= |\mathcal{A}_0|^2 \frac{\alpha_S}{2\pi} c_\Gamma \left(\frac{\mu^2}{m_h^2} \right)^\epsilon \\ &\times \left[-\frac{1}{\epsilon^2} (C_A + 2C_F) + \frac{1}{\epsilon} \left(C_A \left(\ln \frac{s}{m_h^2} + \ln \frac{-t}{m_h^2} \right) - (C_A - 2C_F) \ln \frac{-u}{m_h^2} \right) \right], \end{aligned} \quad (64)$$

where $C_F = (N_c^2 - 1)/2N_c = 4/3$, $C_A = N_c = 3$ and where \mathcal{A}_0 is the tree amplitude given in Eqs. (4) and (7), and $\mathcal{A}_1 \equiv \epsilon_\mu^{h3*}(p_3) \mathcal{A}_1^\mu$ where \mathcal{A}_1^μ is the one-loop amplitude given in Eq. (3). This expression contains both infrared and ultraviolet divergences. The latter are removed

by renormalizing the Yukawa and strong couplings using the counterterms given in Eqs. (61) and (62), respectively. This leaves the infrared-divergent expression

$$\begin{aligned} \left[2\text{Re}(\mathcal{A}_1\mathcal{A}_0^*) + |\mathcal{A}_0|^2 2(\delta y_{\text{RS}} + \delta g_S^{\text{RS}}) \right] \Big|_{\text{div}} &= |\mathcal{A}_0|^2 \frac{\alpha_S}{2\pi} c_\Gamma \left(\frac{\mu^2}{m_h^2} \right)^\epsilon \left[-\frac{1}{\epsilon^2} (C_A + 2C_F) \right. \\ &\quad \left. + \frac{1}{\epsilon} \left(C_A \left(\ln \frac{s}{m_h^2} + \ln \frac{-t}{m_h^2} \right) - (C_A - 2C_F) \ln \frac{-u}{m_h^2} - b_0 - 3C_F \right) \right] , \end{aligned} \quad (65)$$

which has the structure expected from the dipole-subtraction method [30].

We also calculate the relation between the virtual amplitude in CDR and DR. We find

$$2\text{Re}(\mathcal{A}_1\mathcal{A}_0^*)|_{\text{CDR}} = 2\text{Re}(\mathcal{A}_1\mathcal{A}_0^*)|_{\text{DR}} - |\mathcal{A}_0|^2 \frac{\alpha_S}{2\pi} 2C_F . \quad (66)$$

The above relation is consistent with the set of rules given in Ref. [28], augmented by the regularization-scheme-dependent renormalization of the Yukawa coupling given in Eq. (61).

References

- [1] A. Stange, W. J. Marciano and S. Willenbrock, Phys. Rev. D **49**, 1354 (1994) [arXiv:hep-ph/9309294].
- [2] D. A. Dicus and S. Willenbrock, Phys. Rev. D **39**, 751 (1989).
- [3] D. Dicus, T. Stelzer, Z. Sullivan and S. Willenbrock, Phys. Rev. D **59**, 094016 (1999) [arXiv:hep-ph/9811492].
- [4] Z. Kunszt and F. Zwirner, Nucl. Phys. B **385**, 3 (1992) [arXiv:hep-ph/9203223].
- [5] ATLAS Collaboration, Technical Design Report, CERN-LHCC-99-15.
- [6] C. Kao and N. Stepanov, Phys. Rev. D **52**, 5025 (1995) [arXiv:hep-ph/9503415].
- [7] V. D. Barger and C. Kao, Phys. Lett. B **424**, 69 (1998) [arXiv:hep-ph/9711328].
- [8] D. Choudhury, A. Datta and S. Raychaudhuri, arXiv:hep-ph/9809552.
- [9] C. S. Huang and S. H. Zhu, Phys. Rev. D **60**, 075012 (1999) [arXiv:hep-ph/9812201].
- [10] M. Drees, M. Guchait and P. Roy, Phys. Rev. Lett. **80**, 2047 (1998) [Erratum-ibid. **81**, 2394 (1998)] [arXiv:hep-ph/9801229].
- [11] M. Carena, S. Mrenna and C. E. Wagner, Phys. Rev. D **60**, 075010 (1999) [arXiv:hep-ph/9808312].
- [12] J. Dai, J. F. Gunion and R. Vega, Phys. Lett. B **345**, 29 (1995) [arXiv:hep-ph/9403362].
- [13] J. Dai, J. F. Gunion and R. Vega, Phys. Lett. B **387**, 801 (1996) [arXiv:hep-ph/9607379].
- [14] E. Richter-Was and D. Froidevaux, Z. Phys. C **76**, 665 (1997) [arXiv:hep-ph/9708455].
- [15] J. L. Diaz-Cruz, H. J. He, T. Tait and C. P. Yuan, Phys. Rev. Lett. **80**, 4641 (1998) [arXiv:hep-ph/9802294].
- [16] C. Balazs, J. L. Diaz-Cruz, H. J. He, T. Tait and C. P. Yuan, Phys. Rev. D **59**, 055016 (1999) [arXiv:hep-ph/9807349].
- [17] M. Carena *et al.*, Report of the Tevatron Higgs Working Group, arXiv:hep-ph/0010338.
- [18] C. Balazs, H. J. He and C. P. Yuan, Phys. Rev. D **60**, 114001 (1999) [arXiv:hep-ph/9812263].
- [19] W. Beenakker, S. Dittmaier, M. Kramer, B. Plumper, M. Spira and P. M. Zerwas, Phys. Rev. Lett. **87**, 201805 (2001) [arXiv:hep-ph/0107081].
- [20] L. Reina and S. Dawson, Phys. Rev. Lett. **87**, 201804 (2001) [arXiv:hep-ph/0107101].
- [21] F. I. Olness and W. K. Tung, Nucl. Phys. B **308**, 813 (1988).

- [22] R. M. Barnett, H. E. Haber and D. E. Soper, Nucl. Phys. B **306**, 697 (1988).
- [23] M. A. Aivazis, J. C. Collins, F. I. Olness and W. K. Tung, Phys. Rev. D **50**, 3102 (1994) [arXiv:hep-ph/9312319].
- [24] J. C. Collins, Phys. Rev. D **58**, 094002 (1998) [arXiv:hep-ph/9806259].
- [25] T. Stelzer, Z. Sullivan and S. Willenbrock, Phys. Rev. D **56**, 5919 (1997) [arXiv:hep-ph/9705398].
- [26] D. E. Groom *et al.* [Particle Data Group Collaboration], Eur. Phys. J. C **15**, 1 (2000).
- [27] M. Kramer, F. I. Olness and D. E. Soper, Phys. Rev. D **62**, 096007 (2000) [arXiv:hep-ph/0003035].
- [28] Z. Kunszt, A. Signer and Z. Trocsanyi, Nucl. Phys. B **411**, 397 (1994) [arXiv:hep-ph/9305239].
- [29] R. K. Ellis, D. A. Ross and A. E. Terrano, Nucl. Phys. B **178**, 421 (1981).
- [30] S. Catani and M. H. Seymour, Nucl. Phys. B **485**, 291 (1997) [Erratum-ibid. B **510**, 503 (1997)] [arXiv:hep-ph/9605323].
- [31] J. M. Campbell and R. K. Ellis, Phys. Rev. D **62**, 114012 (2000) [arXiv:hep-ph/0006304].
- [32] S. Catani, M. H. Seymour and Z. Trocsanyi, Phys. Rev. D **55**, 6819 (1997) [arXiv:hep-ph/9610553].
- [33] H. L. Lai *et al.* [CTEQ Collaboration], Eur. Phys. J. C **12**, 375 (2000) [arXiv:hep-ph/9903282].
- [34] J. Huston, S. Kuhlmann, H. L. Lai, F. I. Olness, J. F. Owens, D. E. Soper and W. K. Tung, Phys. Rev. D **58**, 114034 (1998) [arXiv:hep-ph/9801444].
- [35] R. K. Ellis *et al.* [QCD Tools Working Group Collaboration], arXiv:hep-ph/0011122.
- [36] M. L. Mangano and S. J. Parke, Phys. Rept. **200**, 301 (1991).
- [37] T. Stelzer and W. F. Long, Comput. Phys. Commun. **81**, 357 (1994) [arXiv:hep-ph/9401258].
- [38] E. Braaten and J. P. Leveille, Phys. Rev. D **22**, 715 (1980).
- [39] M. Beneke and V. M. Braun, Nucl. Phys. B **426**, 301 (1994) [arXiv:hep-ph/9402364].
- [40] I. I. Bigi, M. A. Shifman, N. G. Uraltsev and A. I. Vainshtein, Phys. Rev. D **50**, 2234 (1994) [arXiv:hep-ph/9402360].